

Comparing the low-frequency content of seismic source-receiver combinations using surface-wave analysis: A field case from Hussar, Alberta

Yu-Tai Wu* and Robert R. Stewart*

ABSTRACT

The low-frequency content in seismic exploration is of substantial value as it can benefit imaging and inversion by providing deeper penetration, broader-band energy, wavelet stability, and higher resolution. However, the low-frequency content of the survey source, sensitivity of the receiver, and spectral signal-to-noise character may not be clear. Thus, the interest in their analysis. The Hussar, Alberta survey, conducted by the CREWES Project, addressed this purpose. We further assess the low-frequency content of the Hussar data sets using surface-wave analysis (because of its significant coherent low-frequency energy). The survey tested 2 kg dynamite in addition to vibroseis sources with low-dwell and linear sweeps. The receivers evaluated included Vectorseis accelerometers, 10 Hz, and 4.5 Hz geophones. Our dispersion inversion results indicate that all source-receiver combinations show considerable energy down to about 2 Hz. They also can provide a reasonable V_s estimate to about 300 m, which fits reasonably well with S-wave tomography and well-log measurements. The dynamite source however exhibited the most pronounced low-frequency energy which extended below 1.5 Hz. Low-dwell sweeps showed clearer low-frequency signals than the linear sweep. Among the tested receivers, the 4.5 Hz geophone demonstrated the best low-frequency sensitivity, then Vectorseis accelerometer, and finally the 10 Hz geophone. Using the energy and coherency of surface-wave analysis to access low-frequency content can complement other types of spectral analysis.

INTRODUCTION

Low-frequency generation and analysis in seismic exploration have gained prominence due to their ability to benefit seismic imaging and interpretation with deeper penetration, higher resolution, more stable wavelets, assistance in full-waveform inversion, and more accurate well-log estimation (Martin and Stewart, 1994; Ten Kroode et al., 2013). Numerous studies have demonstrated the advantages of low frequencies in reflection data (Goloshubin et al., 2006; Li and Demanet, 2016). Low frequencies are also of significant benefit in surface-wave analysis.

This study uses the Multichannel Analysis of Surface Waves (MASW) method to evaluate the low-frequency content of different source-receiver combinations from an acquisition test conducted by the CREWES Project in Hussar, Alberta (Margrave et al., 2012). Analysis of surface waves can be a reasonable reference or complement for subsequent studies of other signals to assess usable frequency content. Firstly, surface waves are often the strongest signals. A vertical source, such as a vibroseis, may convert more than half of its energy into surface waves (Woods, 1986). Surface waves also experience less energy loss due to geometrical spreading because they propagate along the

* University of Houston

surface. Moreover, surface waves consist of both P- and S-waves. Evaluating the frequency content of surface waves can provide a reliable reference for other signals, such as P-wave reflections. Lastly, owing to media continuity and a single source in each gather, we can posit that the signals recorded at each receiver represent the same source wavelet with variations in both energy and phase.

In the following sections, we will present the results of the surface wave analysis, compare the Vs models inverted from dispersion curves with other measurements (well-log data and S-wave tomography), and assess the low-frequency signals in the different source-receiver combinations.

Area of study and input data

The research dataset used in this study was obtained from a seismic experiment conducted by the CREWES Project in collaboration with Husky Energy, Geokinetics, and INOVA (Margrave et al., 2012). The primary objective of the experiment was to study low-frequency seismic reflections and test inversion methods. The dataset comprises recordings from a 4.5 km multi-component seismic line near Hussar, Alberta, passing through three wells, as shown in Figure 1.

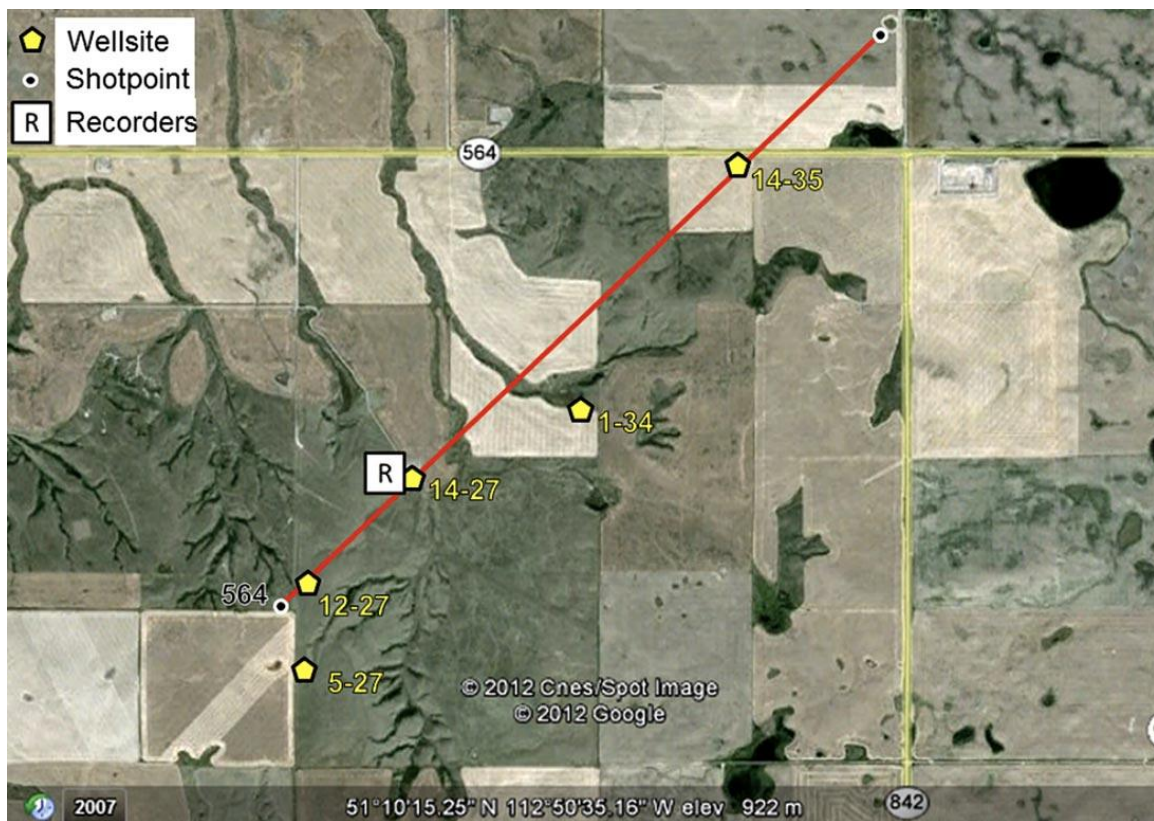


FIG 1. Map view of the 4.5 km Hussar seismic line shown with 5 wells. Only well 12-27 has shear velocity measurements (Margrave et al., 2012).

Various source types were utilized in the experiment, including 2-kg dynamite and vibroseis sources, along with five types of receivers. A specifically modified low-frequency vibrator, the INOVA AHV-IV Model 364, and a more conventional vibrator, the

Eagle Failing Model Y2400, were used. Both vibrators were operated with specially designed low-dwell functions, allocating more time in the frequency range below 8 Hz. The sweeps were 24 seconds long, ranging from 1 Hz to 100 Hz. The low-dwell sweep for the INOVA 364 and Failing vibrators spent the first 10 and 15 seconds on linear sweeping from 1 to 8 Hz. Within the remaining sweep time, the sweeping continued to increase to 100 Hz linearly. A linear sweep from 1 to 100 Hz was also conducted on the INOVA 364 for comparison. Three lines were completely deployed with Vectorseis accelerometers, 10 Hz, or 4.5 Hz geophones. The fourth line, a hybrid configuration, included broadband Trillium seismometers and 10 Hz geophones, spaced at 200 m and 20 m, respectively. The Trillium seismometer data is not discussed in this study due to its inappropriate spacing for the MASW method. In total, the dataset comprises 12 vertical-component lines.

Initial spectral analysis on the reflection signals of the raw data reveals varying levels of low-frequency energy. All four sources in the experiment generated substantial low-frequency energy. The 2-kg dynamite, placed at a depth of 15 m in a single hole, exhibited the highest strength, followed by the INOVA 364 low-dwell, the Failing low-dwell, and the INOVA 364 linear, ranked in decreasing terms of their low-frequency energy output. The Vectorseis accelerometers recorded signals below 1 Hz and had a more sensitive response than the geophones. The 10 Hz and 4.5 Hz geophones performed well down to their resonant frequencies, with signal recovery extending to around 1.5 Hz after inverse filtering for instrument response.

Regarding the surface waves, all receivers showed clear signals in the data, as shown in Figure 2. In the time and frequency domains, the 4.5 Hz geophones exhibited the strongest surface waves and energy in the low-frequency range (<5 Hz).

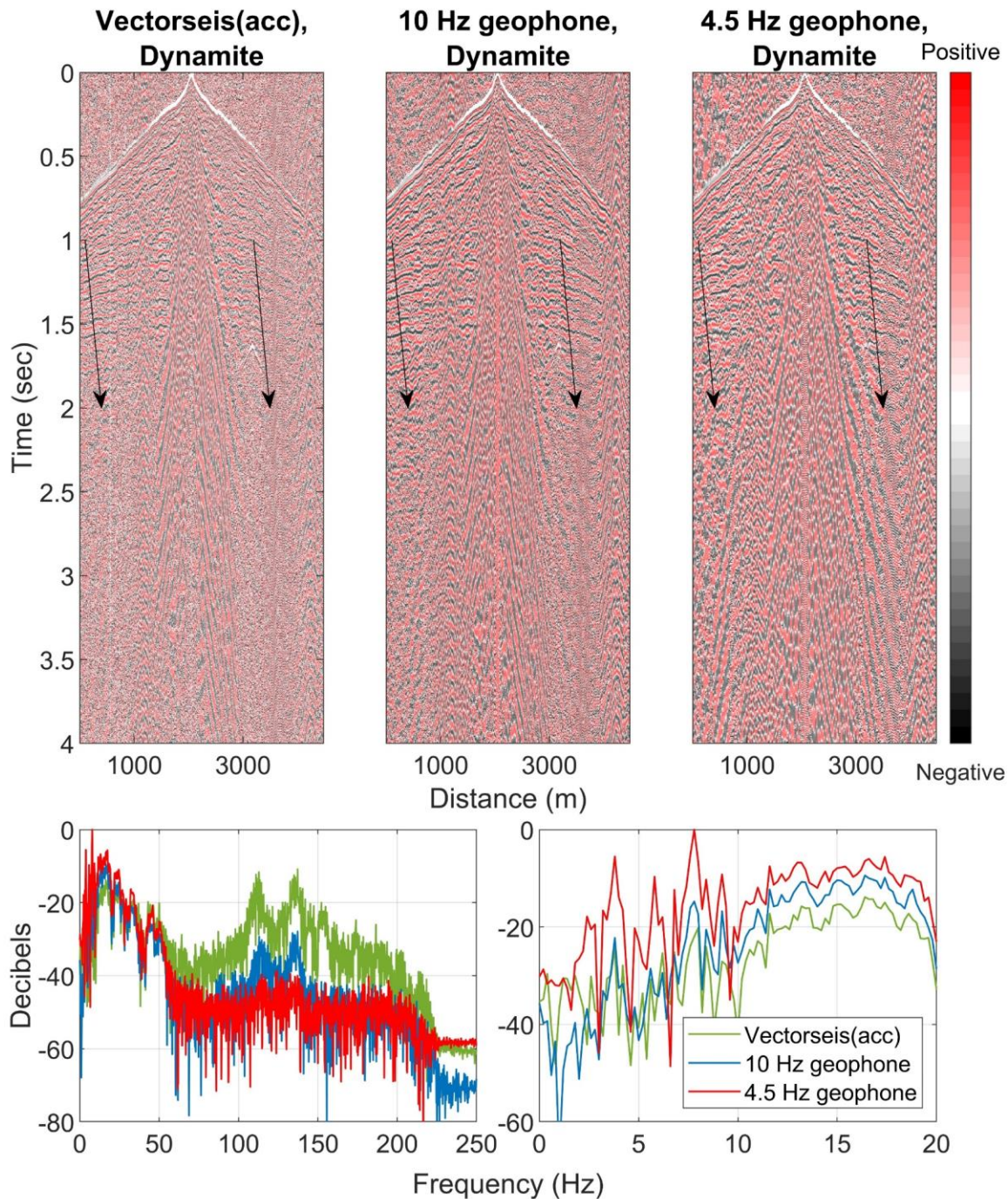


FIG 2. (Top) Seismic data for shot point 321 were generated using 2-kg dynamite and recorded by three types of receivers, including Vectorseis accelerometers, 10 Hz and 4.5 Hz geophones. The images are AGC-applied, with arrows indicating surface waves. The 4.5 Hz geophones have the most apparent surface waves, followed by the Vectorseis accelerometers and the 10 Hz geophones. (Bottom) The spectral analysis result is shown, with an enlarged view in the low-frequency range.

METHODS

Active surface-wave methods can generally be summarized in three key steps: acquisition, processing, and inversion. During the processing stage, the primary objective is to estimate dispersion (that is, velocity versus frequency) curves. Their quality significantly impacts the inverted Vs models. In multi-channel surveys, common methods for dispersion estimation at a Common Midpoint (CMP) include the phase-shift method, f-k, and tau-p transform (Dal Moro et al., 2003). Their sensitivity to phase change decreases with frequency decreasing.

To maintain high sensitivity to phase shift within a short-spread length, we employed the Nonlinear Signal Comparison (NLSC) method within the MASW method, as proposed by Zheng and Hu (2017). Instead of using a single shot for each CMP, we stacked the results to mitigate the influence of acquisition parameters and noise.

In the inversion stage, a 1-D shear velocity mode is estimated based on the dispersion curves (Park et al., 2007). Phase velocities at different frequencies correspond to different wavelengths, resulting in variations in penetration depth. Therefore, low-frequency signals are able to sense deeper layers. The 1-D velocity models are inverted by fitting the dispersion curves obtained from measurements and estimates and are subsequently integrated into 2-D or 3-D models.

Dispersion curve calculation

The NLSC method, as Zheng and Hu (2017) proposed, estimates phase shifts equivalently at different frequencies. It is a two-station method and can effectively mitigate the sensitivity problem in dispersion maps. Following Hu et al. (2019), we stacked the dispersion maps over all sources within a spacing range to improve the identification of modes and suppress noise. Given an angular frequency ω , phase velocity V_{ph} , and a resolution controlling parameter σ , the NLSC method in the MASW method can be expressed as

$$S'_{MNLSC}(\omega, V_{ph}, \sigma) = \sum_{i=1}^{n-1} \sum_{j=1+i}^n \frac{S_{NL}^{ij}(\omega, V_{ph}, \sigma) - S_{\pi}}{1 - S_{\pi}}, \quad (1)$$

where S'_{MNLSC} is a multi-channel result stacked using the results of i-th and j-th traces; n is the number of traces within a confined spread. S_{NL} and S_{π} are the normalized dispersion map and a background value for normalization, respectively; they can be expressed as follows.

$$S_{NL}(\omega, V_{ph}, \sigma) = \frac{1}{T} \int_0^T \exp \left\{ - \frac{\left[\bar{d}_1(t, \omega) - \bar{d}_x\left(t + \frac{x}{V_{ph}}, \omega\right) \right]^2}{4\sigma^2 \omega^2 \pi^{-2}} \right\} dt \quad (2)$$

$$\text{and } S_{\pi}(\omega, \sigma) = I_0(b) e^{-b}, \quad b = \frac{\pi^2}{\sigma^2 \omega^2 T}, \quad (3)$$

in which T is the time window length, x is the receiver spacing, \bar{d}_1 and \bar{d}_x are the seismograms of the two receivers normalized by their variance. S_{π} is defined as two signals with a phase difference of π in S_{NL} , and I_0 is the modified zeroth-order Bessel function.

The stacked dispersion map in Eq. (1) can be further normalized by its maximum and minimum values and ranges from 0 to 1. For detailed derivatives, please refer to Zheng and Hu (2017) and Hu et al. (2019).

$$S_{MNLSC}(\omega, V_{ph}, \sigma) = \frac{S'_{MNLSC}(\omega, V_{ph}, \sigma) - \min [(S'_{MNLSC}(\omega, V_{ph}, \sigma))]}{\max [(S'_{MNLSC}(\omega, V_{ph}, \sigma))] - \min [(S'_{MNLSC}(\omega, V_{ph}, \sigma))]} \quad (4)$$

Modeling and inversion of dispersion curves

The forward modeling of Rayleigh wave dispersion is calculated using the finite-element method, also called the thin-layer method (Kausel 2005). Instead of using displacement potential, this method leads to a linear eigenvalue problem (Haney and Tsai, 2017).

$$k \begin{bmatrix} \mathbf{I} & 0 \\ 0 & \mathbf{B}_2 \end{bmatrix} \begin{bmatrix} \mathbf{v} \\ \mathbf{a} \end{bmatrix} = \begin{bmatrix} 0 & \mathbf{I} \\ \omega^2 \mathbf{M} - \mathbf{B}_0 & -\mathbf{B}_1 \end{bmatrix} \begin{bmatrix} \mathbf{v} \\ \mathbf{a} \end{bmatrix}, \quad (5)$$

where \mathbf{I} is a unit matrix; \mathbf{B}_0 , \mathbf{B}_1 , and \mathbf{B}_2 are the stiffness matrices only comprised of Lamé's constant λ and shear modulus μ . The mass matrix \mathbf{M} only depends on density ρ . Solving the eigenvalue problem, we can obtain eigenvector \mathbf{v} describing the vertical and horizontal nodal displacements and eigenvalue wavenumber k . For a fixed frequency, the phase velocity can be calculated from the relation $k = \omega/V_{ph}$ and the largest eigenvalue corresponds to the fundamental mode.

To invert a 1-D Vs model, we iteratively updated the initial Vs model using the misfit between observed and forward modeling dispersion curves. At fixed frequency, the perturbation in phase velocity caused by model perturbations can be represented as

$$\frac{\delta V_{ph}}{V_{ph}} = \frac{1}{2k^2 U V_{ph} \mathbf{v}^T \mathbf{M} \mathbf{v}} \sum_{i=1}^N \begin{pmatrix} \mathbf{v}^T \frac{\partial(k^2 \mathbf{B}_2 + k \mathbf{B}_1 + \mathbf{B}_0)}{\partial \mu_i} \mathbf{v} \partial \mu_i \\ + \mathbf{v}^T \frac{\partial(k^2 \mathbf{B}_2 + k \mathbf{B}_1 + \mathbf{B}_0)}{\partial \lambda_i} \mathbf{v} \partial \lambda_i \\ - \omega^2 \mathbf{v}^T \frac{\partial \mathbf{M}}{\partial \rho_i} \mathbf{v} \partial \rho_i \end{pmatrix} \quad (6)$$

in which N is the number of modes. The higher modes are included if observed. U is the group velocity and can be calculated from the equation below.

$$U = \frac{\delta \omega}{\delta k} = \frac{\mathbf{v}^T (2k \mathbf{B}_2 + \mathbf{B}_1) \mathbf{v}}{2\omega \mathbf{v}^T \mathbf{M} \mathbf{v}}. \quad (7)$$

RESULTS

The dispersion maps of the same receiver types are compared in Figures 3, 4, and 5 for the Vectorseis accelerometer, 10 Hz geophone, and 4.5 Hz geophone, respectively. They are generated using the stacked NLSC results at a distance less than 100 m from the CMP. The manually picked dispersion curves are overlaid on the maps, with the fundamental mode represented in magenta and the first higher mode in blue. The picking criterion is selecting the phase velocity with the highest correlation coefficient at each frequency. Like the normalized amplitude in the phase-shift method (Park et al., 1998), the correlation coefficient in the NLSC method is used to evaluate the signal quality. The correlation

coefficient for the fundamental mode is presented below the curves in the enlarged figures in the low-frequency range.

An overall comparison is provided in Figure 6, demonstrating a high consistency level in the manually picked dispersion curves. These fundamental-mode dispersion curves fall within the 2 to 8 Hz range, while their first higher modes are between 5 and 10 Hz.

To assess the fidelity of the inversion results, we compared them with other measurements. Fortunately, a well with a shear-velocity log is near the survey line. We also conducted tomography for both P- and S-wave velocities based on picking the first break of P- and S-wave times. They are determined in the vertical and horizontal components, respectively. During inversion, forward estimation is carried out using the Fortran code proposed by Qin et al. (1992), and the initial model is updated iteratively by minimizing misfits using the steepest descent method. The tomography results and the well-log measurements are displayed in Figures 7 and 8. Figures 8A, 8B and 8C compare the dispersion inversion results at the well location with the 1-D Vs models derived from the tomography results and shear-velocity log. These Vs models correspond closely. The dispersion inversion results remain consistent, even when source and receiver types differ. The head waves can only penetrate to a depth of 200 m at this location because of the geometry set, as shown in the Vs model from the tomography result (red line) in the figure. Fortunately, the well log provides shear-velocity data (gray line) starting from 200 m, allowing us to compare Vs models in deeper layers.

Figure 8D shows the average sensitivity kernels for phase velocities in the range of 2 to 6 Hz. It is worth noting that the lowest frequency extending from 2 Hz to 1 Hz has three times increment in the sensitivity depth. Additional log measurements, including Vp, density, and gamma-ray, are presented in Figures 8E and 8F. Formation tops were determined according to Eberth and Brman (2012). In Figure 8F, Poisson's ratio is calculated using the velocities from tomography results and well-log data.

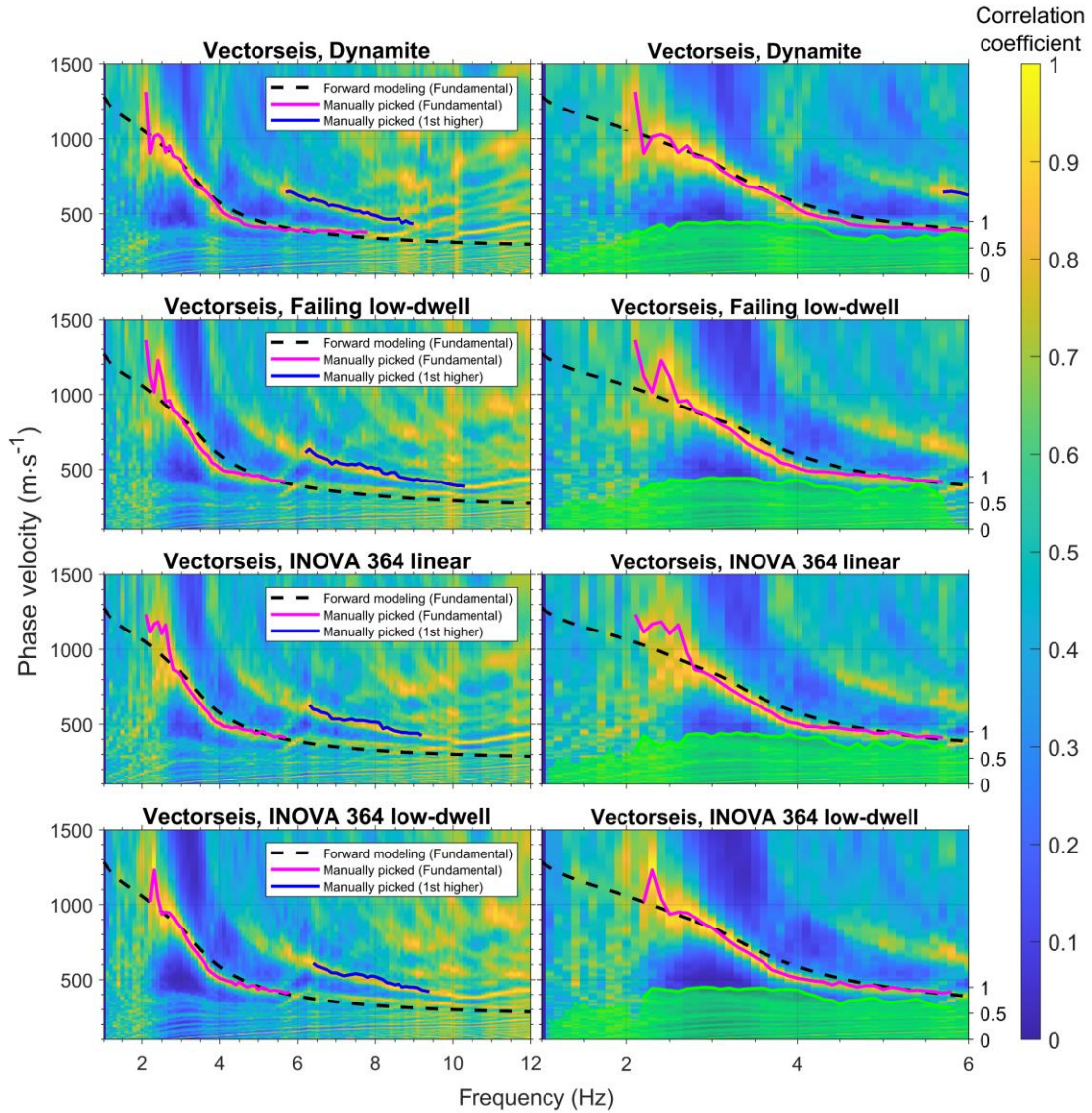


FIG 3. (Left) Dispersion maps of the Vectorseis accelerometer with four different source types. Instrument noise is evident at below 2 Hz. (Right) Correlation coefficients of the fundamental-mode surface wave are displayed, with an enlarged view of the left-column figures in the low-frequency range. The black dotted lines are forward calculated using well-log data and tomography results, helping determine the dispersion curves extending to the frequency below 2 Hz.

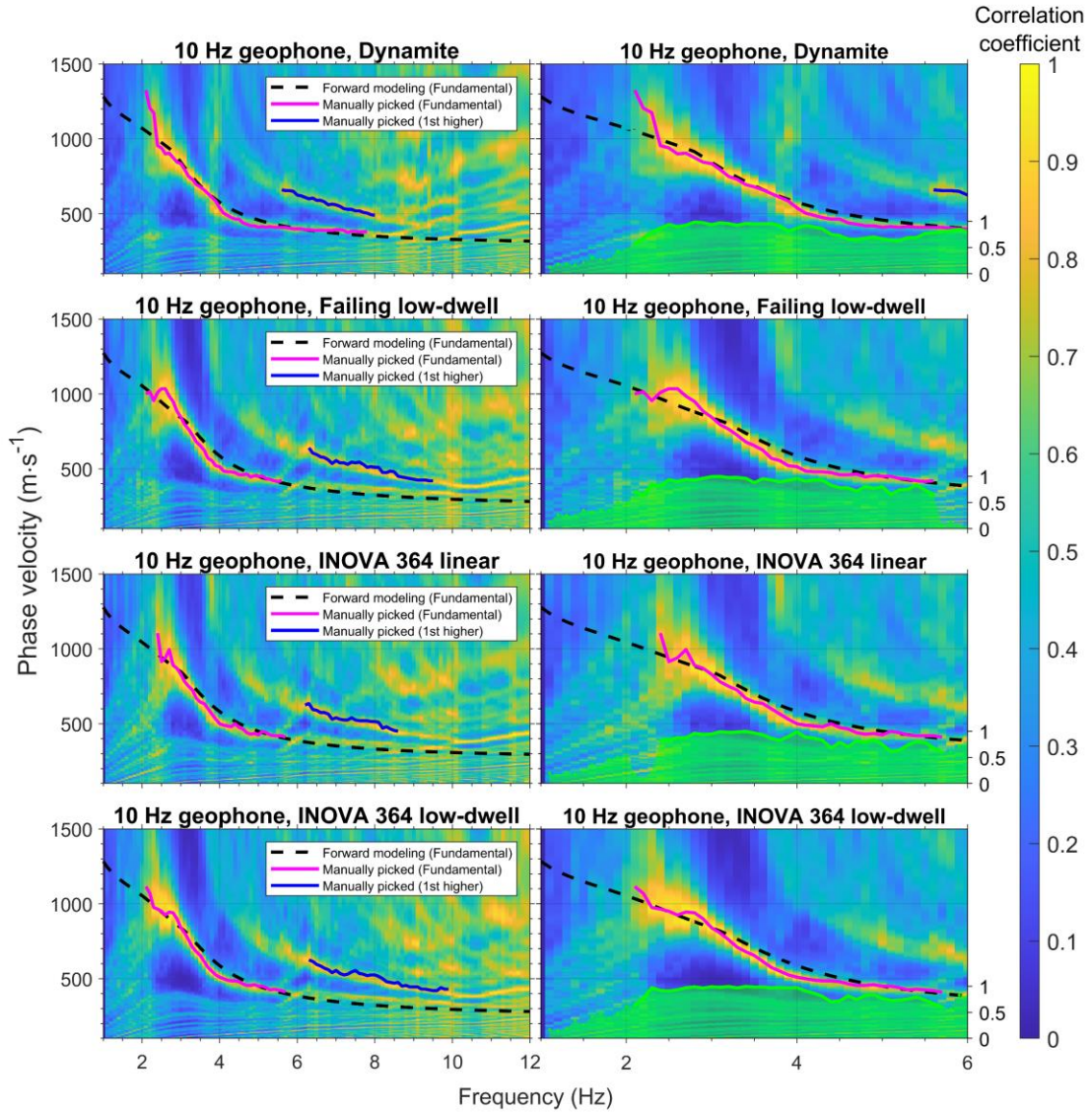


FIG 4. Similar to Figure 3, except that the receivers are 10 Hz geophones.

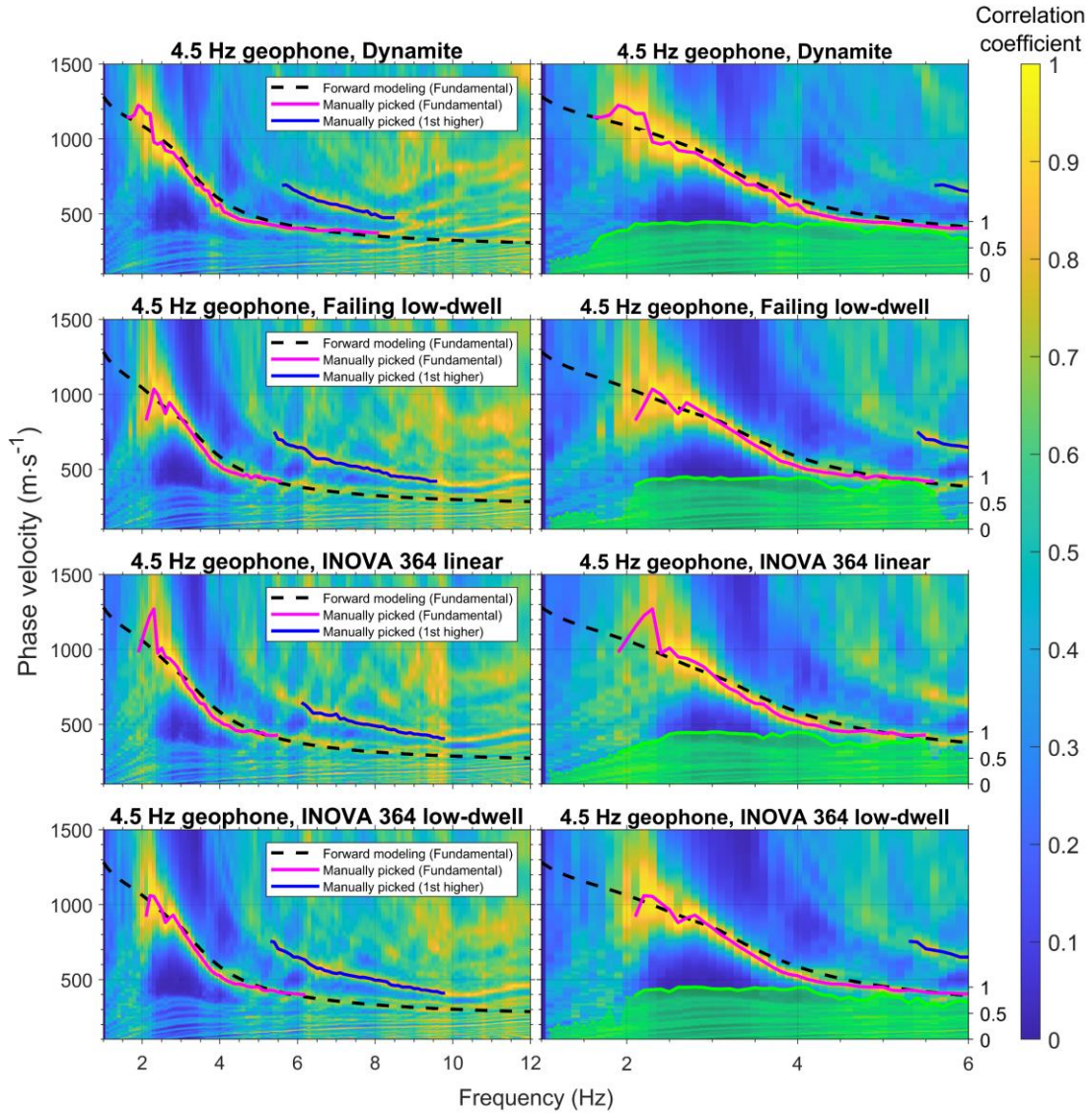


FIG 5. Dispersion maps using data recorded by 4.5 Hz geophones. Dynamite produced the strongest low-frequency energy in the 4.5 Hz geophone recordings among all tested combinations.

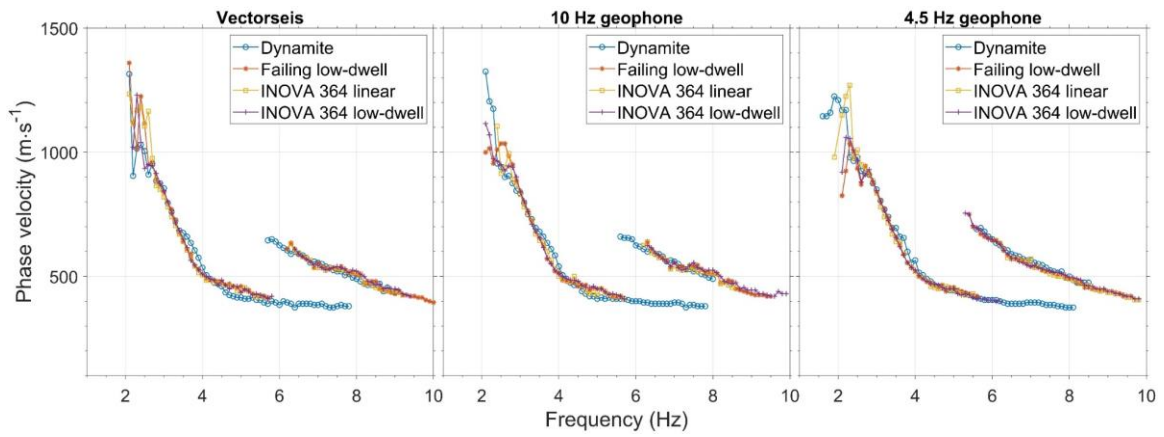


FIG 6. Comparison of manually picked dispersion curves. The high consistency reflects the presence of surface waves in all data sets.

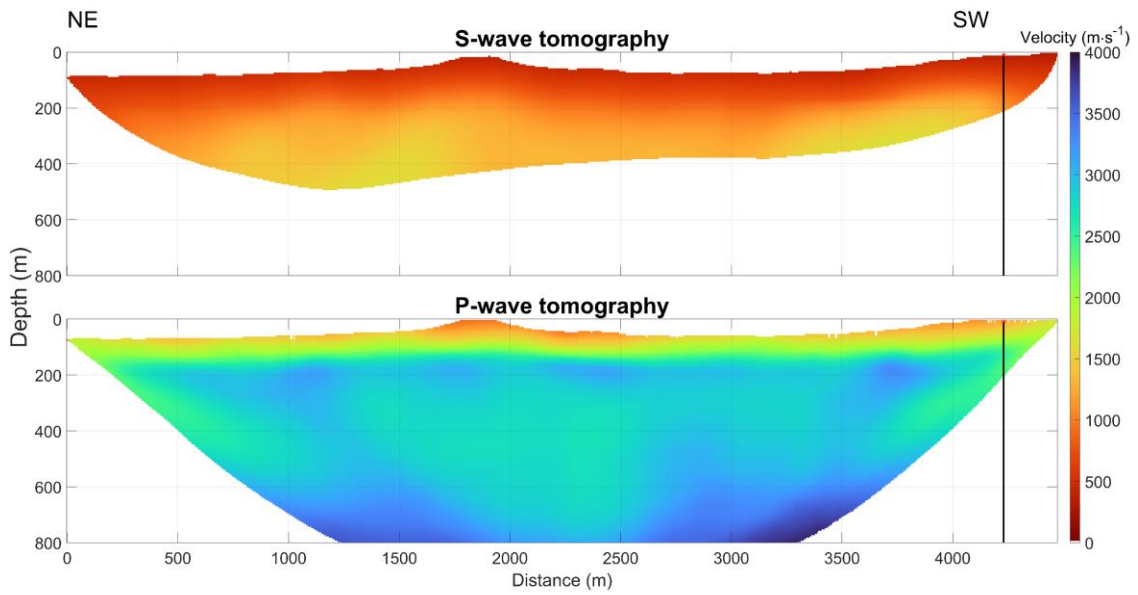


FIG 7. P- and S-wave tomography models. A black line on the tomography models indicates the location of the well log with V_s measurement.

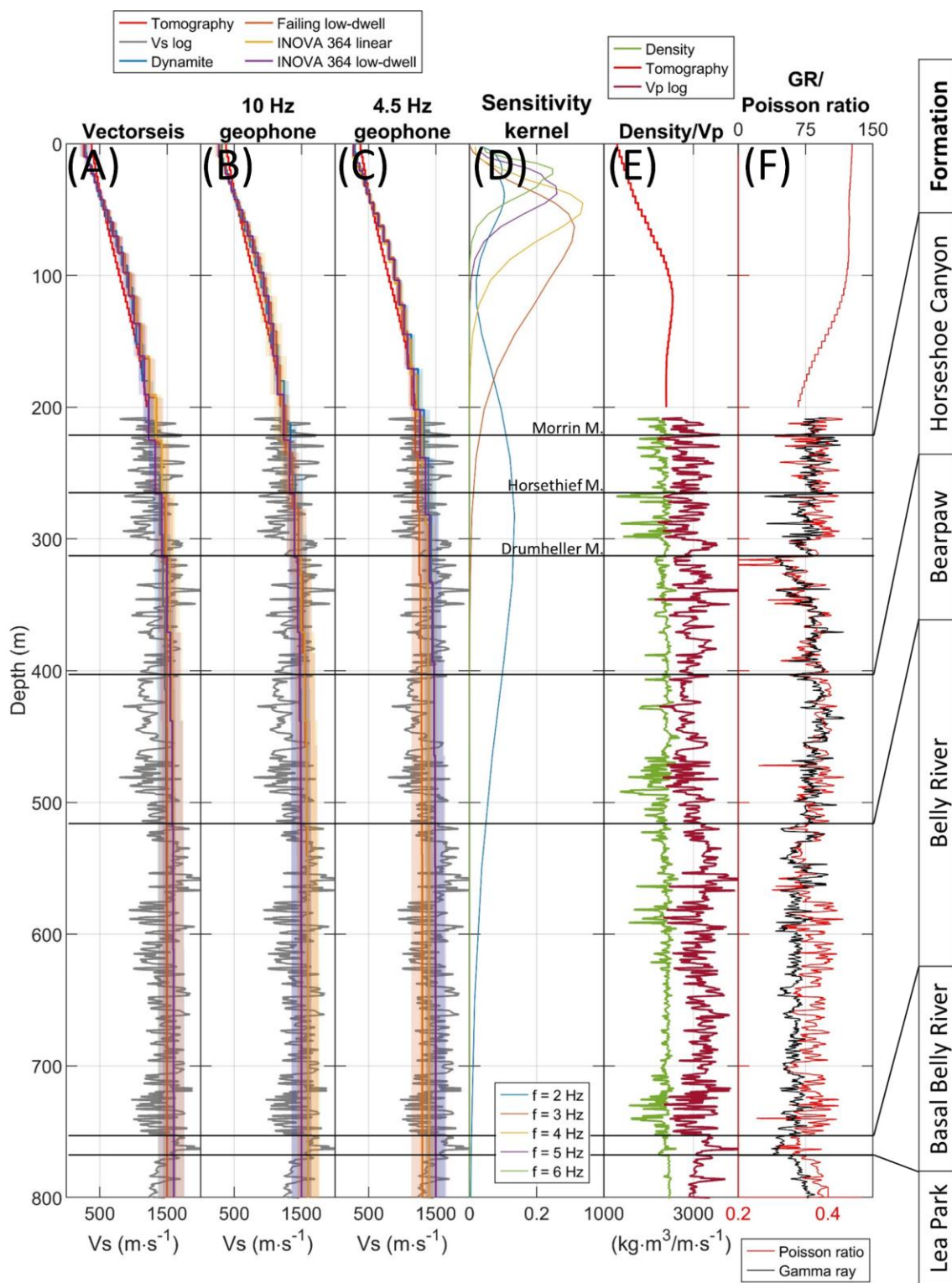


FIG 8. (A, B, and C) Comparison of surface wave inversion results with S-wave log measurements and tomography model. (D) Sensitivity kernels of 2- to 6-Hz surface waves. (E) Acoustic and density logs are shown along with Vp from the tomography model in Figure 7. (F) Gamma-ray log plotted with Poisson ratio calculated from velocities of log measurements and tomography models. Corresponding formation tops at the study site are also shown in all panels.

DISCUSSION

We begin by comparing the quality of the inversion results with other measurements. Subsequently, we evaluate the low-frequency signals in different combinations and contrast the changes in their quality with frequency. We have performed forward estimation using log measurements for dispersion curves below 2 Hz, where they may be unclear. This estimation can provide insights into the potential trends of the dispersion curves. Finally, we contrast the differences between the evaluation of our approach and the spectral analysis of the raw shot data.

Surface-wave inversion

The dispersion inversion results are closely related to the sensitivity depths of the surface waves. Either below or above the depths, the model updates calculated from the phase velocities decrease. The depth D is commonly estimated using the equation below, given a frequency f and phase velocity V_{ph}

$$D = 0.5 \times mode \times V_{ph} \div f \quad (8)$$

in which *mode* represents the number of the harmonic; it is one for the fundamental mode and increases by one for each higher mode. In this study, the maximum sensitivity depth is approximately 300 m, contributed by the 2-Hz signal, as shown in Figure 8D. The average sensitivity kernels also show investigation depth decreases more significantly when low-frequency signals are lost in the data compared to high-frequency signals. As illustrated in Figures 8A, 8B, and 8C, above 300 m, the inverted Vs has less uncertainty than below 300 m and provides more detailed information about velocity changes than travel-time tomography. However, uncertainties increase below 300 m, and the inverted Vs loses some of the details observed in the log measurements. Even so, the dispersion inversion of all combinations offers a reasonable estimation of the shear velocity above 800 m. All the inversion results are similar above 300 m and show slight variations below that depth, but they all fit well with the Vs values obtained from tomography and log measurements.

Low-frequency content evaluation

We conducted a forward estimation of the fundamental-mode dispersion curves to evaluate the low-frequency signals. To calculate phase velocity accurately below 2 Hz, we substituted our inversion results below 200 m with the log measurements. Figures 3, 4, and 5 illustrate the forward curves as black dotted lines.

In Figure 3, the dispersion maps of Vectorseis accelerometers for the four different source types are shown. The surface wave signals extend down to nearly 2 Hz. Below 2 Hz, a high correlation is scarcely visible. Between 2-3 Hz, the dynamite source exhibits the highest correlation coefficients, followed by the INOVA 364 low-dwell, the Failing low-dwell, and the INOVA 364 linear. The ranking order of low-frequency signal quality aligns with the dispersion curve quality. Between 2-3 Hz, the phase velocities picked for the dynamite source best match the forward estimate, while the two low-dwell sweeps start to diverge slightly, and the linear sweep diverges more. Below 2.5 Hz, the picked phase velocities move away from the forward estimates.

Figure 4 presents the same maps for the four source types but recorded by the 10 Hz geophones. Similar source effects are observed, with the difference being that the lowest frequency is around 2.5 Hz, and the overall correlation coefficients below 2 Hz are lower than those in Figure 3. This suggests that the instrument noise of Vectorseis accelerometers may impact the low-frequency signals.

Figure 5 is similar to Figures 3 and 4, with the exception that the receiver is the 4.5 Hz geophone. The configuration of the dynamite and the 4.5 geophone shows the most apparent low-frequency signals among the receivers and sources tested, with dispersion curves fitting well with the forward estimates. Among the other sources, the two low-dwell sweeps generated stronger signals between 2 and 3 Hz than the linear sweep. The lowest frequency is about 1.5 Hz, and no instrument noise is observed.

Our surface wave analysis results show that both geophones can record signals below their natural frequency. The 4.5 Hz geophone can capture signal frequencies down to 1.5 Hz, the Vectorseis accelerometer is less sensitive to signals below 2 Hz, and the 10 Hz geophone primarily records signals above 2.5 Hz. Regarding the sources, dynamite can generate low-frequency signals of at least 1.5 Hz. The sweep functions have a more significant impact than the vibrator models; spending more time sweeping at low frequencies can generate more apparent signals.

Comparison with spectral analysis of raw data

Spectral analysis is a common method for quickly assessing data frequency content at the beginning of the process, as illustrated in Figure 2. While the results are intuitive, they may not always accurately reflect the actual frequency content of the signals. Compared with spectral analysis, surface-wave analysis may provide two advantages. First, it enhances the accuracy of frequency content evaluation by considering signal coherency during the process. Signals are visualized on dispersion maps, and we can determine their phase velocity only when they exhibit coherency at a given frequency. This also allows us to distinguish the instrument noise of Vectorseis accelerometers from the actual signals. Secondly, the results can be cross-verified with other measurements. Although our ranking of suitable receivers and sources for a low-frequency survey aligns with the results of spectral analysis, there is a discrepancy in the lowest frequency that the receivers can record. Surface-wave analysis allows us to visualize the lowest frequency on the dispersion maps, and this can be further examined through forward modeling using other measurements like tomography and well-log data.

CONCLUSIONS

This work has provided a valuable case study for characterizing near-surface properties through surface-wave analysis using low-frequency data down to 1.5 Hz. To assess the reliability of the inversion results, we compared them with well-log measurements and tomography results, which demonstrated close agreement.

Furthermore, our surface wave analysis revealed that low-frequency content was present in all data sets but varied with source and receiver types. Among all source types, dynamite exhibited the strongest low-frequency energy. The type of sweep function had a more significant impact than the vibrator type. The two low-dwell sweeps were nearly identical

in terms of dispersion curves and displayed more pronounced low-frequency signals compared to the linear sweep.

Of the receivers tested, the 4.5 Hz geophone performed the best in displaying low frequencies. When considering the lowest frequency a receiver can record, the Vectorseis accelerometer outperformed the 10 Hz geophone. However, interpreted instrument noise of Vectorseis accelerometers may impact data in the low-frequency range.

Because low frequencies are so useful in seismic analysis, it is important to understand how they can be generated and recorded. This study provides further insight into how best to access and evaluate low frequency seismic data.

ACKNOWLEDGEMENTS

The authors express their appreciation to the CREWES Project, in particular. Dr. Kris Innanen, and its sponsors for providing the Hussar data set for our research. We also thank the Hewlett Packard Enterprise Data Science Institute at the University of Houston for providing computing resources. We are grateful to the Allied Geophysical Lab for its support.

REFERENCES

- Dal Moro, G., Pipan, M., Forte, E., and Finetti, I., 2003, Determination of Rayleigh wave dispersion curves for near surface applications in unconsolidated sediments: *Ann. Internat. Mtg., Soc. Expl. Geophys., Expanded Abstracts*, 1247–1250.
- Eberth, D. A., and Braman, D. R., 2012, A revised stratigraphy and depositional history for the Horseshoe Canyon Formation (Upper Cretaceous), southern Alberta plains: *Canadian Journal of Earth Sciences*, **49**, 1053–1086.
- Goloshubin, G., Van Schuyver, C., Korneev, V., Silin, D., and Vingalov, V., 2006, Reservoir imaging using low frequencies of seismic reflections: *The Leading Edge*, **25**, 527–531.
- Haney, M. M., and Tsai, V. C., 2017, Perturbational and nonperturbational inversion of Rayleigh-wave velocities: *Geophysics*, **82**, F15–F28.
- Hu, H., Senkaya, M., Zheng, Y., 2019, A Novel Measurement of the Surface Wave Dispersion with High and Adjustable Resolution: Multi-Channel Nonlinear Signal Comparison: *J. Applied Geophysics*, **160**, 236–241.
- Kausel, E., 2005, Wave propagation modes from simple systems to layered soils, in Lai, C. G., and Wilmanski K.
- Li, Y. E., and Demanet, L., 2016, Full-waveform inversion with extrapolated low-frequency data: *Geophysics*, **81**, R339–R348.
- Margrave, G. F., Mewhort, L., Phillips, T., Hall, M., Bertram, M. B., Lawton, D. C., Innanen, K., Hall, K. W., and Bertram, K., 2012, The Hussar low-frequency experiment: *CSEG Recorder*, **37**, 25–39.
- Martin, N. and R.R. Stewart, 1994, The effect of low frequencies on seismic analysis: *CREWES Research Report*, 6, 2, 1-8.
- Park, C. B., Miller, R. D., and Xia, J., 1998, Imaging dispersion curves of surface waves on multi-channel record: *Ann. Internat. Mtg., Soc. Expl. Geophys., Expanded Abstracts*, 1377–1380.
- Park, C. B., Miller, R. D., Xia, J., and Ivanov, J., 2007, Multichannel analysis of surface waves (MASW)—active and passive methods: *The Leading Edge*, **26**, 60–64.
- Qin, F., Luo, Y., Olsen, K. B., Cai, W., and Schuster, G. T., 1992, Finite-difference solution of the eikonal equation along expanding wavefronts: *Geophysics*, **57**, 478–487.
- Ten Kroode, F., Bergler, S., Corsten, C., de Maag, J. W., Strijbos, F., and Tijhof, H., 2013, Broadband seismic data—The importance of low frequencies: *Geophysics*, **78**, WA3–WA14.
- Woods, R.D., 1968, Screening of surface waves in soils: *J. Soil Mechanics and Foundation Division*, **94**, 951–979.

Zheng, Y., and Hu, H., 2017, Nonlinear signal comparison and high-resolution measurement of surface wave dispersion: *Seismol. Soc. Am.*, **107**, 1551–1556.